Water mass structure of wind forced river plumes

ROBERT D. HETLAND

Department of Oceanography, Texas A&M University, College Station, TX

Submitted to *J. Physical Oceanogr.* on March 15, 2004

Abstract

The water mass structure of a river plume is examined using an idealized numerical model of fresh water discharging from an estuary into a continental shelf. It is shown that the river plume may be divided into two distinct regions, categorized by the dominant mixing processes in each zone. The near-field region is where the river plume undergoes active mixing as the estuary discharge spreads and entrains background water through shear mixing. The far-field region is where mixing by the wind is the dominant mechanism for entraining background water into the plume. Entrainment of background waters is greatest in the near-field, where the salt flux is . Shear mixing due to the wind will only mix the upper buoyant layer to a point, after which turbulence due to shear mixing is suppressed. Approximating the plume as a single layer appears to be valid over most of the plume.

1. Introduction

River plumes are central in a number of important oceanographic problems. For example, a toxic dinoflagellate, *Alexandrium spp.*, is associated with the the Kennebec/Penobscot river plume in the Gulf of Maine (Franks and Anderson, 1992). Stratification caused by Mississippi/Atchafalaya outflow prevents ventilation of lower layer waters, allowing hypoxic conditions to develop on the continental shelf (Rabalais et al., 1999). Nearly half of all oceanic carbon burial occurs in large river deltas (Hedges and Keil, 1995). If we wish to better understand and predict these biogeochemical systems, we must first improve our understanding of the underlying physical system.

River plumes are, by nature, nonlinear due to the importance of advection of buoyant water and turbulent mixing. The flow within the plume may be supercritical, indicating advection is an important part of the momentum balance, particularly near the estuary mouth. Advection is also essential to the tracer balances, as the plume changes position. Turbulent mixing is essential for entraining background water into the plume and eventually mixing the plume into the ambient waters of the continental shelf.

Because of this inherent non-linearity, analytic models of river plume dynamics have often focused only on particular aspects of the flow field, such as an inviscid pulse of water flowing from a river (e.g., O'Donnell, 1990; Garvine, 1987) or examined mixing of an established plume by the wind (Fong and Geyer, 2001). Most recent theoretical work on river plumes has considered the plume as as a single active buoyant layer, supporting analytical calculations with numerical models. Theoretical predictions using a single active layer have been compared to three-dimensional numerical simulations of buoyant outflow (e.g., Yankovsky and Chapman, 1997; Fong and Geyer, 2001), numerical reduced gravity models (e.g., O'Donnell, 1990; Nof and Pichevin, 2001), and laboratory results (e.g., Lentz and Helfrich, 2002).

Many simulations of idealized river plumes do not consider the effects of wind. In these simulations, a bulge forms at the mouth of the estuary (Yankovsky and Chapman, 1997; Fong, 1998; Yankovsky, 2000; Nof and Pichevin, 2001). Because this bulge is typically not seen in either observations or numerical simulations with wind forcing, it is often considered an artifact, and an undesirable aspect of the numerical solutions (e.g., Garvine, 2001). Inclusion of wind stress in the idealized simulations usually removes the bulge, and produces what is argued to be a more realistic solution (Fong and Geyer, 2001; García Berdeal et al., 2002). Simulations using realistic domains and forcing have demonstrated that wind is essential in reproducing observations of river plumes (Pullen and Allen, 2000; Hetland and Signell, submitted). This suggests wind is an essential ingredient in producing a realistic numerical simulation of a river plume. However, it should be noted that other idealized studies have obtained what was considered to be a more realistic solution by changing the model domain (Garvine, 2001) or other forcing parameters (Yankovsky et al., 2001).

The purpose of this paper is to employ idealized numerical simulations of a wind forced river plume to identify dynamically distinct regions within the river plume, quantify entrainment of ambient water into the plume, and assess the validity of approximating the plume as a single, active layer. These objectives are related in that the regions are identified by the dominant entrainment process, and each region is treated conceptually as a single, active layer. Analysis of the plume is done in salinity coordinates, a more natural coordinate system for the river plume than Cartesian coordinates. Salinity coordinates use the water mass structure of the plume to examine the plume as a whole, by tracking fresh water introduced from the river through the plume to it's eventual fate as it it mixed into the background waters.

Wind stress amplitude is chosen as the primary variable parameter, due to the importance of wind in creating realistic river plume simulations. Regions in the plume are separated by different vertical mixing processes. Close to the estuary mouth, advective shear mixing caused by shoaling of the buoyant outflow is the dominant mixing process. Outside of this region, wind mixing created by vertical shear at the base of the Ekman layer is the dominant mixing process. In salinity coordinates, a layer model captures the essential structure of entrainment of ambient water into the plume in both of these regions.

In section 2, the numerical setup and physical configuration are described. The basic findings of numerical sensitivity studies are presented in section 3. In section 4, I describe theoretical aspects of analysis methods used. Results, including descriptions of the near- and far-field regimes of the plume, are presented in section 5. These results are discussed in section 6, with concluding remarks in section 7.

2. Numerical setup

The simulations employ version 2.0 of the Regional Ocean Modeling System (ROMS, Haidvogel et al., 2000). ROMS is a free-surface, hydrostatic, primitive equation ocean model that uses stretched, terrain-following coordinates in the vertical and orthogonal curvilinear coordinates in the horizontal. The code design is modular, so that different choices for advection and mixing, for example, may be applied by simply modifying preprocessor flags.

The numerical domain is a narrow estuary attached to a uniformly sloping shelf with a straight coastline (figure 1). The resolved oceanic part of the domain is approximately 250 km long, and 80 km wide, with variable resolution concentrated near the estuarine outflow region, and along the coast. Resolution is decreased near the edges to inhibit small-scale along-shore variability at the northern and southern boundaries.

The estuary is 10 m deep, approximately 20 km long, and 1.5 km wide. Fresh water is introduced as a boundary condition on the westward end. Tides are not explicitly modeled. Tidal mixing within the estuary is parameterized by specifying a constant diffusivity/viscosity of 1×10^{-4} m^2 s^{-1}, so that the length scale of the salt intrusion is not significantly greater than the channel length, and the timescale

of estuarine adjustment is rapid enough to come into a steady state within approximately one upwelling/downwelling period (Hetland and Geyer, sion). The coastal ocean has a 10 m wall along the coast, and the bottom has a uniform slope of 1/1500, resulting in a maximum depth at the eastern boundary of about 70 m.

Garvine (2001) suggests that model configuration is important in influencing some of the aspects of simulated river plumes. In particular, he notes that maintaining a very shallow depth at the coast prevents the formation of a backward propagating (against the Kelvin wave propagation direction) bulge at the estuary mouth. Practically, the shallowest possible coastal wall depths are a few tens of centimeters in models like ROMS that do not support wetting and drying. In this study, the coastal wall is 10 m deep, instead of near zero as Garvine's study suggests. I have chosen not to use a shallow coastal wall for two reasons. First, even in the cases with no wind and no background flow (not shown here), a backward propagating bulge was not a problem. Second, it is not clear how the very shallow water near the coast might influence the plume when a wind stress is applied. Austin and Lentz (2002) show how the Ekman layer may be shut down on a stratified shelf under wind forcing when the near-shore water becomes vertically well mixed, trapping water in the shallow region near the coast. In other simulations in which the topography was kept very shallow along the coast (not shown here) this caused a portion of the plume to be trapped near the coast, even when the plume was upwelled. Although this effect may be real, it is not well understood, particularly in terms of how this trapped water will influence the water mass modification in the plume as a whole.

The model is initiated with no flow and a flat sea surface. The initial tracer distribution is uniform background salinity of 32 psu, with vertical temperature stratification typical for an east coast continental shelf in summer (a 10 m homogeneous mixed layer above exponential stratification with a 20 m decay scale, ranging from 20°C at the surface to 5°C at depth). The plume never interacts directly with the thermocline. The estuary was initialized with a vertically uniform along-channel salt gradient, linearly transitioning from oceanic salinity to fresh water over 50 km, in order to decrease the estuarine adjustment time. The model is forced with fresh water at the river end of the estuary and spatially uniform but temporally oscillating north-south wind stress; both are ramped with a hyperbolic tangent function with a 12 hour timescale (figure 2). The depth integrated flow at the eastern boundary is set equal to the Ekman transport.

The northern boundary (the upstream boundary in the Kelvin wave sense) depth integrated flow is relaxed to results from a two-dimensional experiment to prevent drift in the along-shore transport through the domain. In experiments without this boundary condition, the transport averaged over an upwelling/downwelling cycle tended to drift $\mathcal{O}(0.10\ \mathrm{m\ s^{-1}})$. The two-dimensional experiment has no mass flow into the domain from the river, but identical wind stress. The domain is identical, except that it is periodic in the north-south direction, with the same cross-shore topography as the three-dimensional simulations. The flow is initially at rest, with no sea surface height anomalies. The eastern boundary transport is again set to the Ekman transport. Any mean along-shore background

flow is added to the two-dimensional results before they are applied to the three-dimensional model.

In the three-dimensional experiments, mass is conserved except for the gain and loss of mass due to the Ekman transport by requiring the northern and southern boundaries carry the same along-shore transport. This is accomplished by integrating the flow along these two boundaries, then applying a small transport along all open boundaries to correct any mass transport imbalances.

The physical configuration for the basic case is a fresh water flux of 1000 m^3 s^{-1} applied at the river end of the estuary, and a spatially uniform, oscillatory in time, along-shore wind stress with an amplitude of 0.0, 0.2, or 0.5×10^{-4} m^2 s^{-2} and a period of 4 days, shown in figure 2. A mean background current, flowing in the Kelvin wave propagation direction, of -0.05 m s^{-1} is specified at the northern boundary (in addition to the two-dimensional wind-driven transport). The archetype for this configuration is the Kennebec River plume in the Gulf of Maine, which has been the subject of a number of observational and numerical studies (Fong et al., 1997; Hetland and Signell, submitted; Geyer et al., in revision).

The numerical configuration uses fourth-order Akima horizontal advection for tracers with a grid-scaled horizontal diffusivity equivalent to 0.04 m^2 s^{-1} for a 1 km^2 grid cell (ranging from 0.02 to 0.2 m^2 s^{-1} in the resolved portion of the domain). A third-order, upwind scheme is used for horizontal momentum advection, with no explicit horizontal viscosity applied. The model has 20 vertical s-layers, with resolution focused near the surface (s-coordinate parameters used are h_c = 10 m, θ_s=5.0, and θ_b=0.01). This is equivalent to better than 1 m vertical resolution in the upper 5 meters of the water column over the entire domain. Conservative splines are used to estimate vertical gradients. Vertical mixing was estimated using the Mellor-Yamada turbulence closure scheme. Moderate horizontal resolution, 500 m resolution in the immediate vicinity of the outflow, results in three grid points across the estuary mouth.

This configuration was chosen to balance numerical accuracy with computational speed. This type of configuration could be applied to a realistic river plume simulation without significant modifications to the standard code, and with reasonable integration time on modern computers. It takes about nine hours of wall clock time to integrate the simulation for a month on a single 2.3 GHz Intel Itanium processor.

Results for this configuration are shown in figure 3. The upper panels show sea surface salinity with surface currents overlaid, and lower panels show the fresh water thickness for the final four days of the simulation. Fresh water thickness, relative to a reference salinity, s_0, is defined as the vertical integral of the salinity anomaly, $(s_0 - s)/s_0$ (see equation 9 below). The plume changes position considerably over one cycle of the wind stress forcing. During upwelling, the plume nearly loses contact with the coast, a trait that becomes more pronounced as the duration of upwelling increases. During downwelling, the plume is pressed against the coast, developing a strong coastal current. The plume's response to upwelling and downwelling is not symmetric: during upwelling the plume is blown offshore, during downwelling the plume is pushed along-shore. This causes most of the

along-shore fresh water flux to occur during downwelling conditions; along-shore fresh water flux is essentially halted during upwelling.

3. Numerical sensitivity

Numerical sensitivity experiments were performed to understand the numerical requirements and limitations of the simulations described in this paper, and the general findings are presented below. Because these runs are idealized, the numerical sensitivity studies focused on internal consistency between model results. In order to do this, a grid-converging method was used, in which resolution is increased until the properties of the solution do not change. The implicit assumption is that there are no systematic model errors, that as resolution is increased the solution converges to the true solution.

Fresh water volume within different salinity classes is used in order to examine changes in whole plume structure. The fresh water volume, relative to the reference salinity, s_0, is defined as the integral of the fresh water fraction

$$V_f(s_A) = \iiint_{s<s_A} \frac{s_0 - s}{s_0} dV, \tag{1}$$

where the volume integral is bounded by the isohaline s_A, such that all of the water fresher than s_A is contained in the integral. In order to determine the distribution of fresh water as a function of salinity class, $\partial V_f / \partial s_A$ is plotted for various numerical configurations. This may be used to compare how different numerical schemes affect plume water mass structure. Integrating $\partial V_f / \partial s_A$ over a range of salinities will give the total fresh water contained within those salinity classes. As mixing increases, fresh water will generally be moved toward higher salinity classes.

Numerical resolution and advection scheme Generally, adequate numerical resolution is found to be the most important component for a consistent solution. In particular, resolution needs to be high enough near the estuary mouth in order to resolve the outflow. As might be expected, grid convergence begins at 3-5 grid cells across the estuary mouth, depending on the other numerical algorithms. Figure 4 shows the fresh water volume distribution for three different choices of resolution near the estuary mouth. The grids resolving the estuary mouth with three and five grid points gave similar results, whereas the grid resolving the estuary mouth with a single grid point (a common practice in realistic modeling) did not result in two distinct water masses, and had slightly different volumes of water at higher salinities.

Plume dimensions, such as bulge diameter, are surprisingly insensitive to advection scheme, providing the domain has adequate resolution near the estuary mouth. The qualitative structure of the solution is always the same, even using poor resolution and a low-order advection scheme. All of the simulations (without wind) have a bulge forming directly downstream of the estuary outflow.

The largest difference between advection schemes is in the formation of spurious fresh and dense water. Numerical over- and undershoots in the vicinity of the front would create slightly saltier and fresher water on both sides of the front. The fresh water is lighter than the surrounding water, and remains at the surface. However, the saltier water is denser than the surrounding water and sinks. This artificial unmixing creates a pool of salty water along the sea floor, as well as a spurious source of fresh water near the surface. Because, in the simulations presented in this paper, background salinity is constant, the magnitude of the spurious fresh water source may be calculated by equating it to the spurious, salty bottom water. In simulations with poor resolution, using a third-order advection scheme, no horizontal mixing, and the KPP vertical closure, the spurious fresh water source reaches nearly 10% of the real, specified fresh water source. The spurious fresh water source can be reduced by applying a moderate horizontal mixing. Using higher resolution and a more diffusive vertical mixing scheme (Mellor-Yamada, see below), even the relatively weak horizontal mixing used in the simulations presented here reduces the spurious fresh water flux to essentially nil. The spurious fresh water flux is 0.5% of the specified fresh water flux over the continental shelf region with no wind forcing, and 0.05% with wind forcing. Traditionally in coastal numerical modeling, it is assumed that horizontal mixing should be kept as low as possible without degrading the solution, and this convention has been followed here. However it has not been demonstrated that this actually produces results more consistent with observations.

Turbulence closure The differences in plume water mass structure between different grid resolutions and advection schemes are dwarfed by the differences in water mass structure using different vertical closure schemes. The primary mixing process in the simulations presented here is shear mixing. Fortunately, this is a process that all modern turbulent closure algorithms contain in some way. Unfortunately, slight differences in the parameterization of shear mixing can be amplified over the history of a water parcel, so that the resulting water mass distribution can be substantially different, depending on the choice of mixing parameterization. Also, all second-order closure schemes (like Mellor-Yamada, $k-\epsilon$, $k-\omega$, and GLS) are based on boundary layer physics. When buoyancy forcing is strong, and wind forcing is weak, this may be a bad approximation for mixing in a river plume.

Three different fresh water distributions are shown for three commonly used turbulent mixing closures: Mellor-Yamada, $k-\epsilon$, and KPP (Mellor and Yamada, 1974; Large et al., 1994; Umlauf and Burchard, 2003). The parameters used were the default parameters for each particular scheme. Although the qualitative structure is similar between the different closure schemes, there are differences in the amount of fresh water found at high salinity classes (figure 5). Notably, the $k-\epsilon$ closure seems to mix the most along the plume, while the KPP closure mixes least. The Mellor-Yamada closure was chosen as the base for this study because it has a long history in coastal ocean modeling, and because it seemed to be a good compromise between the relative extremes represented by the other closure schemes.

It should be noted, however, that this choice is arbitrary. An observational basis for choosing a particular scheme (or scheme parameters) is desperately needed.

4. Theory

a. Salt flux across isohaline surfaces

Interpreting measurements of a river plume in Cartesian space may be difficult, for instance the plume may be only occasionally present at certain locations. The analysis methods presented below are less sensitive to the motions of the plume, because these methods consider the water mass structure of the plume as a whole using a coordinate system based on salinity. This salinity-based coordinate system follows the plume as it moves and allows the fresh water introduced into the domain to be followed as it is mixed with the background waters. The analysis presented below is based on the approach of MacCready et al. (2002), who examine long-term estuarine salt balances by calculating salt fluxes across isohalines. In particular, the derivation below shows how isohaline surface area can be related to salt flux estimates at particular salinity classes within the plume.

Here, we will consider a volume, V, bounded by the sea surface and ocean floor, a face within the river where $s = 0$, and on the seaward edge by an isohaline, s_A (the shaded area in figure 6). A portion of the bounding area, A, defined by the isohaline surface s_A, completely divides fresher plume water ($s < s_A$) from the rest of the ocean. There is a net fresh water flux of Q_R across the face of the volume within the river.

The three-dimensional salt balance equation,

$$\frac{\partial s}{\partial t} + \nabla \cdot (s\mathbf{u}) = -\nabla \cdot \mathbf{f}, \tag{2}$$

integrated over volume, V, is

$$\frac{\partial}{\partial t}\int_V s\ dV - s_A \int_A \mathbf{u_A} \cdot d\mathbf{A} + s_A \int_A \mathbf{u} \cdot d\mathbf{A} = -\int_A \mathbf{f} \cdot d\mathbf{A}, \tag{3}$$

where $\mathbf{u}$ is the three-dimensional flow vector, $\mathbf{u_A}$ is the normal velocity of the surface A itself (such that $\mathbf{u} - \mathbf{u_A}$ is the flow through A), and $\mathbf{f}$ is the diffusive salt flux. The generalized Leibnitz Theorem (Kundu, 1990, page 75) is used to take the time derivative outside the integral in the first term. Both the advective and diffusive salt fluxes are zero on all surfaces of V, except on the surface defined by A. Because s_A is defined to be constant along A, s_A may be taken outside the area integrals. A statement of mass balance within the volume, again derived by integrating over V, is

$$\frac{\partial V}{\partial t} - \int_A \mathbf{u_A} \cdot d\mathbf{A} + \int_A \mathbf{u} \cdot d\mathbf{A} = Q_R. \tag{4}$$

The mass and salt balance equations are combined to form

$$s_A \frac{\partial}{\partial t} V_{fA} = s_A Q_R + \int_A \mathbf{f} \cdot d\mathbf{A}, \tag{5}$$

where

$$V_{fA}(s_A) \equiv \int_V \frac{s_A - s}{s_A}\, dV \tag{6}$$

is the fresh water content within V, relative to s_A. If equation 5 is divided by s_A, an intuitive fresh water balance is formed – the fresh water from the river, Q_R, must either increase V_{fA} in time, or be compensated by a fresh water flux, $\mathbf{f}/s_A$, across A.

By knowing Q_R and the change in fresh water content over time, the *average* salt flux, $\bar{\mathbf{f}}$ across A may be estimated. However, it is expected that within the river plume the flux will change at different points within the plume, so that an area average of the salt flux over a large isohaline may be difficult to interpret: are changes in average flux due to the inclusion of a single hot-spot of mixing, or representative of more broad-scale changes?

Because the pycnocline of the plume is thin, the salt flux across two isohalines within the pycnocline will be similar. The assumption of a thin pycnocline may be used to derive an estimate of the salt flux as at a particular salinity class, instead of as an average across an entire isohaline surface. In particular, assume that the plume is approximated as a single, active layer with horizontally varying salinity overlying a quiescent layer with a uniform, background salinity of s_0. The area, A, may now be related exactly to surface salinity alone, by

$$A(s_A) = \iint_{s<s_A} dA \Big|_{z=\eta}. \tag{7}$$

In this case, A completely contains areas associated with fresher water, and is contained completely by the areas associated with higher values of s_A. Because of this, $A(s_A)$ is a monotonically increasing function, with a well defined inverse.

The integral over A may be converted to an integral over s_A by converting dA to $\frac{\partial A}{\partial s} ds$. Differentiation equation 5 with respect to s_A gives

$$\frac{\partial}{\partial t} \frac{\partial}{\partial s_A} (s_A\, V_f) = Q_R + f_A\, \frac{\partial A}{\partial s_A}, \tag{8}$$

where f_A is the average vertical salt flux associated with salinity class s_A. If equation 8 is multiplied by $\partial s_A / s_A$, it becomes a *local* statement of the fresh water balance at salinity class s_A, just as equation 6 becomes a *global* statement of the fresh water flux after dividing by s_A.

Differentiating with respect to salinity is not intuitive. A steady state version of equation 8 may be derived heuristically by taking the difference of equation 5 evaluated at two neighboring isohalines, s_A and $s_A - \delta s$. Because the pycnocline is thin, the salt flux across the overlapping area is identical. Here, f_A is the average salt flux over δA, the difference in the two areas considered (see figure 6). In the limit where $\delta s \to 0$, the steady state form of equation 8 is recovered.

b. Critical plume thickness

Away from the mouth of the estuary, mixing in the plume is due primarily to surface wind stress. The basic mechanism was described by Fong and Geyer (2001), who describe a one-dimensional model in which a buoyant layer is mixed by shear mixing. The shear between the upper and lower layers is created by the Ekman transport of the upper layer. If the Ekman transport is large enough to induce shear instability in the upper layer, it will mix, entraining lower layer water until the Richardson number is lowered to sub-critical values. Fong and Geyer calculated the depth at which this criteria would be reached, based on a density difference between the upper and lower layers and a specified wind stress. In their calculation, the upper layer density was approximated as constant.

This theory can be extended to include density changes in the upper layer due to entrainment of lower layer water. Consider a layer of purely fresh water, with density ρ_f and h_f thick, overlaying denser (ρ_0) ocean water, infinitely deep. A wind stress, τ, blows over the water causing an Ekman transport in the upper layer of $uh = \tau/\rho_0 f$, where u is the velocity in the upper layer and h is the upper layer thickness. The upper layer may undergo shear mixing, and entrain water from the underlying ocean when the Bulk Richardson number, $Ri = \Delta\rho g h/\rho_0 \Delta u^2$ (where $\Delta\rho$ is the density difference, and Δu the velocity difference between the two layers), becomes lower than a critical value Ri_c. Now, allow the density of the upper layer to decrease as deeper water is entrained, so that $h_f\,\Delta\rho_f = h\,\Delta\rho$, where $\Delta\rho_f = (\rho_f - \rho_0)$ is the density difference between fresh water and the reference state, and

$$h_f \equiv \int_{-H}^{\eta} \frac{s_0 - s}{s_0}\, dz \tag{9}$$

is the fresh water thickness. Solving for $h = h_c$, the critical upper layer thickness when $Ri = Ri_c$, gives

$$h_c = \frac{2\tau}{\rho_0 f}\sqrt{\frac{Ri_c}{h_f\, g\, \Delta\rho_f/\rho_0}} = \frac{h_f}{4\, Ri_c\, F_d^2}, \tag{10}$$

stating that the final upper layer thickness depends only on the initial conditions, the value of Ri_c, and the magnitude of the (maximum) wind stress. This equation may be cast in terms of an upper layer, fresh water Froude number, $F_d = u_{Ekman}/c_f$, where $u_{Ekman} = \tau/f\rho_0 h_c$ and $c_f = \sqrt{h_c g \Delta\rho_f/\rho_0}$. This upper layer, fresh water Froude number is similar to the densimetric Froude number often used in studies of estuarine circulation (e.g., Hansen and Rattray, 1966; MacCready, 1999).

Equation 10 may be converted to a critical salinity by conserving the total fresh water in the water column ($h_f = h_c \Delta s/s_0$) to get

$$s_c = s_0\left(1 - \frac{h_f}{h_c}\right) = s_0(1 - 4\, Ri_c\, F_d^2). \tag{11}$$

If the local salinity in the plume is less than s_c, mixing will occur, if the local salinity is greater than s_c, the water column is stable.

Equation 10 was derived assuming a slab-like upper layer, with constant velocity and density. If the layer is considered to have uniform gradients, as in Fong and Geyer (2001), there will be an additional $2^{-1/2}$ factor on the right hand side. However, changes such as this are equivalent to changes in the critical bulk Richardson number, and do not change the dynamical meaning of the equation.

5. Results

In this section, the plume is shown to have two dynamically distinct regions, referred to here as the near- and far-fields. Water that leaves the estuary passes through both of these regions sequentially before it is mixed into the background flow field, so that each region influences the total water mass structure of the plume in a unique way. Because of this, changes in mixing (caused by real processes or numerical errors) in near field may cascade to the far field.

The near field plume is mixed by advective processes near the mouth of the estuary, and is persistent regardless of the wind state. In a way, this region is an extension of the estuary, as mixing in this region will depend primarily on the estuary outflow properties, and the geometry of the river mouth. The far field is dominated by mixing by the wind. The mixing process is similar to that described by Fong and Geyer (2001), with entrainment of water included so that the density of the upper layer may change.

a. Near-field

As the estuary outflow leaves the confines of the estuary channel, the flow in the upper layer expands and entrains denser water until the Richardson number and the Froude number reach sub-critical values (Wright and Coleman, 1971; MacDonald, 2003). This region represents a rapid transition between the estuary outflow and the plume water beyond the near-field, that will mix at a much slower rate in the absence of wind.

Figure 7 shows the properties of the plume with no wind forcing on day 16 of the simulation. By this time a bulge has formed near the outflow, with a recirculating gyre. The bulge grows in time; as noted by Fong (1998), only a portion of the fresh water introduced continues downcoast as a coastal current. In the case presented here, about half of the fresh water input into the domain is carried away by the coastal current. Because of this, fresh water accumulates within this bulge, and the bulge expands and thickens.

A weighted average of the vertical salt flux ($\langle \kappa \partial s / \partial z \rangle$, defined by equation 15 below), is plotted in the third panel of figure 7, and is used to estimate the regions where vertical mixing is strong. There is a region of strong vertical mixing near the estuary outflow about two orders of magnitude larger than the vertical mixing found in the rest of the plume. When the distribution of maximum vertical salt flux is compared to the Froude number (the fourth panel in figure 7), it is apparent

that the region of high mixing is associated with supercritical flow. The Froude number in the upper layer is defined operationally here as

$$Fr_1 = \frac{u_1}{g' h_1} \tag{12}$$

where

$$u_1 = \int_{-h_1}^{\eta} |\mathbf{u}| dz, \quad g' = \frac{\rho_0 - \rho_1}{\rho_0}, \quad \text{and} \quad \rho_1 = \int_{-h_1}^{\eta} \rho |\mathbf{u}| dz \Big/ \int_{-h_1}^{\eta} |\mathbf{u}| dz, \tag{13}$$

and the upper layer thickness, h_1, is defined as the point where $\rho = \frac{1}{2}(\rho_0 - \rho_{min})$. The subscript one represent average property values in the upper layer. The depth dependent flow speed in the upper layer is $|\mathbf{u}|$, the depth dependent density is ρ. The integrations are over the upper layer, between the free surface and the interface defined by h_1. The upper layer density is weighted by the flow speed to be consistent with a layer model.

The numerically simulated near-field outflow region has a similar structure to that described by Wright and Coleman (1971), where the flow from South Pass of the Mississippi Birdfoot Delta is shown to rapidly shoal at the mouth of the pass, with Froude numbers over two just past the point where the pycnocline shallows during ebb tide. Beyond this point, the flow decelerates and becomes saltier due to entrainment of denser, sluggish background waters. In approximately eight to ten channel widths (depending on the phase of the tide) the South Pass outflow has entrained enough background water so that the Froude number is below one.

The results of Armi and Farmer (1986) suggest that the estuarine outflow will be supercritical. This will occur even when the estuarine exchange is not maximal (Stommel and Farmer, 1953). The simulated estuarine exchange is not maximal (Hetland and Geyer (in revision) argue this is not expected for a prismatic estuary channel), but the simulated upper layer outflow is supercritical near the mouth of the estuary. Thus, the simulated estuarine outflow is similar to flow through a constriction in the case where only the upper layer flow becomes supercritical (e.g., the bottom three panels in Figure 2 of Armi and Farmer (1986)). One notable difference is that Armi and Farmer (1986) show a relatively gradual transition to higher Froude numbers, with a rapid transition back to subcritical flow in the form of a hydraulic jump. In the numerical simulations presented here, as well as in the results of Wright and Coleman (1971), the transition to supercritical flow by shoaling of the pycnocline is relatively rapid (occurring over less than 1 km) compared to the gradual transition back to subcritical flow through mixing (occurring over approximately 5 km).

b. Far-field

The critical thickness of the plume as a function of fresh water thickness an wind stress (equation 10) suggests that wind mixing may act to stabilize the water mass structure of the plume. Even if the upper layer is mixed by some other

mechanism before the maximum in wind stress occurs, wind mixing will still mix the upper layer to the same thickness, so long as h_c is larger than the thickness of the upper layer after the initial mixing. However, this assumes that the horizontal distribution of fresh water is given. It is likely that this distribution is in some ways related to the water mass structure itself. For instance, vertical thickness of the mixed layer will determine the speed of the Ekman transport in the upper layer, and density anomalies between the plume and the background flow will determine the propagation speed of the coastal jet.

If, on the other hand, the plume has already been mixed to or beyond the critical thickness, the plume will not mix further. This mixing could be caused by a previous large wind event, for example. In this case, the theory suggests that the plume will be shielded from the effects of the wind mixing; the water mass structure of the plume will be determined by the largest previous wind event.

To examine how well this theory can predict the salinity structure of a river plume, the plume sea surface salinity was compared to the estimated critical salinity in the upper layer. In figure 8, the simulated sea surface salinity is compared to the critical upper layer salinity calculated from equation 10 (noting that $h_f\, S_0 = h\, \Delta S$) using the local fresh water thickness and $Ri_c = 3.0$. During maximum upwelling, there is a band of sea surface salinity that is proportional to the predicted critical upper layer salinity, plus a 5 psu offset. The relatively high value of Ri_c may be required because mixing in the plume is controlled not only by shear mixing of the upper layer Ekman flow, but also by mechanical stirring by the wind that can enhance the shear mixing. Also, there may be geostrophic or advective flow in addition to the Ekman flow, enhancing shear in the upper layer. Locations in the plume that have a salinity greater than the critical salinity are associated with lower mixing. This suggests that portions of the plume are indeed shielded from wind mixing. During downwelling, nearly all of the plume has subcritical values of surface salinity, and strong vertical mixing is confined to fresher waters in the near-field region.

c. Average salt flux over one upwelling/downwelling cycle

After the plume has reached a quasi-steady state, the average entrainment into the plume over an upwelling/downwelling cycle can be calculated from the steady state form of equation 8,

$$f_A = Q_R \left(\frac{\partial \bar{A}}{\partial s_A} \right)^{-1}, \tag{14}$$

where $\bar{A}$ is the average area contained within isohaline s_A over one upwelling/-downwelling cycle.

A direct estimate of the salt flux is calculated using the turbulent salt flux calculated within the model, again averaged over one upwelling/downwelling cycle. The vertical turbulent salt flux is integrated from the ocean floor to the sea surface, and is weighted by the vertical salinity gradients to give

$$\left\langle \kappa \frac{\partial s}{\partial z} \right\rangle = \frac{\int_{-h}^{\eta} \kappa \left(\frac{\partial s}{\partial z}\right)^2 dz}{\int_{-h}^{\eta} \frac{\partial s}{\partial z} dz}, \tag{15}$$

where κ is the turbulent diffusivity calculated within the model. The weighting is used to get an estimate of the salt flux across the entire pycnocline that may be compared directly a layer model estimate of the salt flux.

A comparison between f_A and $\left\langle \kappa \frac{\partial s}{\partial z} \right\rangle$ is shown in figure 9. The two estimates show the same structure, with high salt flux in the near-field where shear mixing is strong, decreasing by nearly an order of magnitude at higher sanities, where wind mixing is the dominant entrainment process. The two estimates are most different very near the estuarine outflow, where the assumption of a single, active layer may not be valid. Beyond this point, both estimates of salt flux are similar to within the noise of the estimates throughout the near- and far-field, from 18 to 30 psu.

d. Time dependent water mass properties

Time dependent calculations of fresh water volume, sea surface salinity area, and fresh water thickness are plotted versus salinity class in figure 10. This figure shows how the water mass structure and other characteristics of the plume evolve through an upwelling/downwelling wind stress cycle.

In the case with no wind two components of the plume with distinct water mass properties are apparent: the bulge, most notable as a local high in sea surface salinity area and fresh water thickness, and the coastal current portion of the plume at higher salinities. Both the local peak in fresh water volume and sea surface salinity area, as well as the local high in fresh water thickness, are pushed toward higher salinity classes as the magnitude of the wind forcing becomes stronger, a result also seen in figure 5.

As the amplitude of the wind stress increases, a local maximum in fresh water thickness develops at intermediate salinity ranges, beginning at a salinity typical of the bulge in the case with no wind forcing, and persisting through to the point where fresh water volume and plume area become large. The maximum fresh water thickness in the near field occurs after maximum downwelling. The maximum in fresh water thickness also correspond to maxima of fresh water volume and plume surface area for those salinity classes. This indicates a build-up of fresh water. During upwelling this water is transfered to higher salinity classes through shear mixing.

As expected, the amount of fresh water in each salinity class is inversely proportional to the corresponding vertical salt flux. In figure 10, the vertical salt flux is calculated from equation 8. Water leaving the near-field has a salinity of about 22 psu. This water is moved toward higher salinity classes during one distinct period in the upwelling/downwelling cycle: just after upwelling. This water is mixed to a salinity class where the average mixing is much smaller, where there is a low in the critical salinity scaled by the local salinity.

During upwelling, the plume spreads out and thins, decreasing not only the physical plume thickness but also the fresh water thickness, h_f. As h_f decreases,

the upper layer, fresh water Froude number, F_d, decreases causing the critical upper layer salinity, s_c, to increase (see equations 10 and 11). Thus, as the portion of the plume at a particular salinity class thins, it may become susceptible to mixing by the wind if the critical salinity becomes larger than the salinity class in question.

The moderate wind case ($\tau = 0.2 \times 10^{-4}$ m^2 s^{-2}) has characteristics of both the no wind case ($\tau = 0.0$ m^2 s^{-2}), and strong wind case($\tau = 0.5 \times 10^{-4}$ m^2 s^{-2}). Two water distinct water masses are apparent in the moderate wind case, just as in the no wind case. In the moderate wind case, the fresher slug of water, at approximately 25 psu, is mixed into the higher salinity classes during upwelling. This is similar to the high wind case, when the majority of water is moved to high salinities during upwelling. It seems that there is a smooth transition to a plume that is not affected by wind to a plume strongly influenced by the wind, although three points in this parameter space are not enough to resolve the details of this transition.

e. Salinity space cross-section

Treating the plume as a single active layer effectively collapses the vertical dimension. Here, the vertical dimension is retained, and the plume is collapsed along a horizontal dimension using salinity space.

An average vertical salinity profile was calculated as a function of sea surface salinity. This was accomplished by averaging the vertical water mass structure underneath each sea surface salinity class. The distance along-plume in salinity space was calculated by taking the square-root of the area enclosed by each sea surface salinity contour. The results are shown as a salinity space profile (figure 11).

The pycnocline is generally thinner than the overlying mixed layer, supporting the single active layer approximation. Both the near- and far-field can been seen in the salinity space cross-section, but the estuary has a volume that is too small to be seen clearly in this calculation. The plume thickens after it leaves the estuary, between approximately 5 and 20 km, or up to a surface salinity of 26 psu. Beyond the near-field, the plume maintains a fairly constant thickness. As sea surface salinity increases, this is equivalent to a decreasing fresh water thickness. At very high salinities, above 31 psu, the plume thickens considerably, as it merges with the background oceanic water.

The plume structure remains similar though different phases of the wind stress. The salinity space profile, like a profile in physical space, does change with the phase of the wind stress: the plume becomes longer and thinner during upwelling, shorter and thicker during downwelling. The length of the plume varies by approximately 15%, and the thickness by about a factor of two between upwelling and downwelling.

6. Discussion

a. Plume structure

These results discussed in the previous section can be combined to form a view of the fresh water as it flows through the plume. The estuarine outflow ranges from 15 to 18 psu, with higher salinity outflow during higher wind stress. As the surface layer thins, the flow becomes supercritical and mixes in the near-field region. Water leaving the near-field has a salinity of approximately 21 to 22 psu in the simulations with no wind. This water recirculates within the bulge that forms just downstream, in the Kelvin wave sense, of the estuarine outflow, creating a thick, homogeneous mass of water within the bulge. In the periphery of the bulge, which eventually forms the coastal current region downstream of the bulge, the upper layer is thinner, current speeds are higher, and mixing is enhanced compared to that within the bulge. Beyond the bulge, in the coastal current region, mixing is weak, and the coastal current maintains a nearly constant along-shore structure.

In the simulations with strong wind ($\tau = 0.5 \times 10^{-4}$ m^2 s^{-1}), water still leaves the near-field region at approximately 21 to 22 psu. However, wind mixing affects water down to a salinity class of 18 psu, especially during upwelling, so mixing in the near-field is enhanced by the presence of the wind. During periods of weak wind, water begins to build up at mid-range salinity classes between 22 to 28 psu. During upwelling, this water is moved toward higher salinity classes as it is mixed, ending up in the bulk of the plume, at a salinity class range of 28 to 30 psu. At this point, the plume seems to be shielded from the effects of wind mixing. In the simulations shown here, it may take two wind stress cycles (eight days total) for the water that left the near-field to obtain a salinity representative of the far-field plume.

b. The potential stabilizing effects of wind stress

Wind stress may act to stabilize the water column by actively mixing the plume only to a particular point. Equation 10 and the corresponding analysis presented in figure 8 suggest that wind mixing will be strong until the plume has reached a particular critical thickness, after which mixing will decrease. This critical thickness depends on the magnitude of the wind stress and the equivalent fresh water thickness. Given the same horizontal fresh water thickness distribution, the plume will mix to the same end member independent of mixing history. So if poor numerical resolution causes more or less mixing in the near-field region, wind mixing may compensate for this error as long as the critical thickness (or corresponding upper layer salinity) has not yet been reached. However it is not clear that this mechanism will always give the same water mass characteristics, as the horizontal distribution of fresh water may be affected by the near-field flow, background circulation, phasing of the wind stress, and other changes to the forcing field.

Garvine (2001) notes that steady-state along-shore scale of a river plume without wind forcing depends on, among other things, the value of background mixing

used. Background mixing is used to specify a minimum value for diffusivity and viscosity in a turbulence closure scheme. The results of this paper suggest that wind mixing may reduce or eliminate the disconcerting dependence of the plume structure on background mixing. Because Garvine's simulations did not contain wind, strong mixing was contained to the estuary and the near field. After water has left this region, stratification reduces turbulent mixing, so that vertical diffusivity is close to or at background values. In a steady state, all of the fresh water input into the system through the river must pass through each isohaline in the plume. In order for isohalines beyond the near-field mixing region to pass this fresh water through at background values of diffusivity, the surface area of that isohaline must be large. If the background diffusivity is reduced by half, the surface area must double to compensate, so that the fresh water flux through the surface remains constant. Wind mixing increases the mixing at all salinity classes below 30 psu (see figure 8), thereby decreasing the dependence on background mixing.

Using this line of reasoning, the steady state (or time-averaged) surface area of an isohaline will be inversely proportional to the average mixing across that isohaline. Thus, even if the dependence of the plume spatial scales on the background mixing have been reduced, the dimensions of the plume still depend on the amount of mixing within the plume. Different mixing schemes that vary slightly in the magnitude of mixing in the pycnocline will produce plumes of different scales, as noted in section 3. So, although differing in details, this study confirms Garvine's basic result that plume structure depends fundamentally on the mixing parameterization.

7. Conclusions

The water mass structure of an idealized river plume was examined in the context of changing wind stress amplitude. The plume can be divided into two dynamically distinct regions, the near-field in which advective shear mixing was dominant and the far-field in which wind mixing was dominant. Mixing within the plume, caused by primarily by advective shear mixing but also by wind stress, is related to the surface area of isohalines within the plume. Given the same fresh water flux, strong mixing requires only a small isohaline area whereas weaker mixing requires a larger isohaline area. Strong mixing is confined to the near-field of the plume where advective shear mixing is important. Wind mixing is strongest during upwelling when the plume thins and the fresh water thickness decreases, causing the critical salinity to increase so that the plume becomes more suceptable to wind mixing.

A reasonable approximation to the plume structure is a single active layer in which salinity may vary horizontally within the layer, but the pycnocline is very thin everywhere. A single layer approximation may be used to obtain an estimate of the salt flux across the pycnocline that has the same characteristics as a direct estimate using a weighted average of the vertical salt flux. This estimate of the salt flux is accurate in the far-field region, but is not exact in the near field, especially very close to the estuary mouth. A layer model may also be used to estimate a

critical salinity, dependent on the local fresh water thickness and wind stress. The critical salinity was an upper bound on the surface salinity through most of the domain, except for a few grid points very the estuary outflow. This suggests that the majority of the plume, particularly the far-field, is shielded from wind mixing.

A cartoon of the plume shown in figure 12 demonstrates the mixing history of a water parcel as it leaves the river/estuary, and eventually becomes part of the background waters. Water leaves the estuary, and rapidly entrains water in the near-field due to shear mixing of the inertial flow field. If there is a wind stress applied to the plume, there will also be mixing along the frontal regions of the plume. Water that is not near a front may be shielded from further mixing by the wind. The plume water in these interior regions has already been mixed to a critical thickness by previous wind events, so that further entrainment due to shear mixing in the upper layer is suppressed.

The numerical setup used for the simulations presented here would be straightforward to implement in most modern numerical ocean models, even as part of a broader coastal modeling effort. One of the difficulties in comparing numerical simulations of river plumes to observations is that river plumes change position, so at any given point, the plume may be present only some of the time. Because the analysis presented in this paper focuses on distributions of salinity, the analysis methods may be applied to both numerical output and hydrographic observations (providing the measurements resolve the thin surface plume). Salinity coordinates offer an integrative view of the plume that does not depend on small changes in frontal position, may therefore be used to supplement more conventional model/data comparisons based in geographic space.

Acknowledgments

I would like to thank Parker MacCready for many helpful comments and suggestions. This project was supported by ONR project N00014-03-1-0398.

References

Armi, L. and D. M. Farmer (1986). Maximal two-layer exchange through a contraction with barotropic net flow. *J. of Fluid Mech. 164*, 27–51.

Austin, J. A. and S. J. Lentz (2002). The Inner Shelf Response to Wind-Driven Upwelling and Downwelling. *J. Phys. Oceanogr. 32*(7), 2171–2193.

Fong, D. A. (1998). *Dynamics of Freshwater Plumes: Observations and Nuerical Modeling of the Wind-forced Response and Alongshore Freshwater Transport*. Ph. D. thesis, Joint Program in Oceanography, MIT/WHOI.

Fong, D. A. and W. R. Geyer (2001). Response of a river plume during an upwelling favorable wind event. *J. of Geophys. Res. 106*(C1), 1067–1084.

Fong, D. A., W. R. Geyer, and R. P. Signell (1997). The wind-forced response of a buoyant coastal current: Observations of the western Gulf of Maine. *J. of Marine Systems 12*, 69–81.

Franks, P. J. S. and D. M. Anderson (1992). Alongshore transport of a toxic phytoplankton bloom in a buoyancy current: *Alexandrium tamarense* in the Gulf of Maine. *Marine Biology 112*, 153–164.

García Berdeal, I., B. M. Hickey, and M. Kawase (2002). Influence of wind stress and ambient flow on a high discharge river plume. *J. of Geophys. Res. 107*(C9), 13–1–13–24.

Garvine, R. W. (1987). Estuary Plumes and Fronts in Shelf Waters: A Layer Model. *J. of Phys. Oceanogr. 17*, 1877–1896.

Garvine, R. W. (2001). The impact of model configuration in studies of buoyant coastal discharge. *J. of Marine Res. 59*(2), 193–225.

Geyer, W. R., R. P. Signell, D. A. Fong, J. Wang, D. M. Anderson, and B. A. Keafer (in revision). The Freshwater Transport and Dynamics of the Western Maine Coastal Current. *Cont. Shelf Res.*.

Haidvogel, D. B., H. Arango, K. Hedstrom, A. Beckmann, P. Malanotte-Rizzoli, and A. Shchepetkin (2000). Model Evaluation Experiments in the North Atlantic Basin: Simulations in Nonlinear Terrain-Following Coordinates. *Dyn. Atmos. Oceans 32*, 239–281.

Hansen, D. V. and M. Rattray (1966). New dimensions in estuary classification. *Limnol. Oceanogr. 11*, 319–326.

Hedges, J. I. and R. G. Keil (1995). Sedimentary organic matter preservation: an assessment and speculative synthesis. *Marine Chemestry 49*, 81–115.

Hetland, R. D. and W. R. Geyer (in revision). An idealized study of dynamically controlled estuarine scales. *J. Phys. Oceanogr.*.

Hetland, R. D. and R. P. Signell (submitted). Modelling coastal current transport in the Gulf of Maine. *Deep-Sea Res. II*.

Kundu, P. (1990). *Fluid Mechanics*. Academic Press.

Large, W. G., J. C. McWilliams, and S. C. Doney (1994). Oceanic vertical mixing: A review and a model with a nonlocal boundary layer parameterization. *Reviews of Geophysics 32*(4), 363–403.

Lentz, S. J. and K. R. Helfrich (2002). Buoyant Gravity Currents Along a Sloping Botton in a Rotating Fluid. *J. of Fluid Mech.*.

MacCready, P. (1999). Estuarine Adjustment to Changes in River Flow and Tidal Mixing. *J. of Phys. Oceanogr. 29*(4), 708–729.

MacCready, P., R. D. Hetland, and W. R. Geyer (2002). Long-Term Isohaline Salt Balance in an Estuary. *Cont. Shelf Res. 22*, 1591–1601.

MacDonald, D. G. (2003). *Mixing Processes and Hydraulic Control in a Highly Stratified Estuary*. Ph. D. thesis, MIT/WHOI.

Mellor, G. L. and T. Yamada (1974). A heirarchy of turbulent closure models for planetary boundary layers. *J. Atmos. Sci. 31*, 1791–1806.

Nof, D. and T. Pichevin (2001). The ballooning of outflows. *J. of Phys. Oceanogr. 31*, 3045–3058.

O'Donnell, J. (1990). The Formation and Fate of a River Plume: A Numerical Model. *J. of Phys. Oceanogr. 20*(4), 551–569.

Pullen, J. D. and J. S. Allen (2000). Modeling Studies of the Coastal Circulation off Northern California: Shelf Response to a Major Eel River Flood Event. *Cont. Shelf Res. 20*, 2213–2238.

Rabalais, N. N., R. E. Turner, D. Justic, Q. Dortch, and W. J. Wiseman (1999). Characterization of Hypoxia: Topic 1 Report for the Integrated Assessment on Hypoxia in the Gulf of Mexico. Technical report, NOAA Coastal Ocean Program, Silver Spring, MD.

Stommel, H. and H. G. Farmer (1953). Control of salinity in an estuary by a transition. *J. Mar. Res. 12*(1), 13–20.

Umlauf, L. and H. Burchard (2003). A generic length-scale equation for geophysical turbulence models. *J. Mar. Res. 61*, 235–265.

Wright, L. D. and J. M. Coleman (1971). Effluent Expansion and Interfacial Mixing in the Presence of a Salt Wedge, Mississippi River Delta. *J. of Geophys. Res. 76*(36), 8649–8661.

Yankovsky, A. E. (2000). The cyclonic turning and propagation of buoyant coastal discharge along the shelf. *J. of Marine Res. 58*, 585–607.

Yankovsky, A. E. and D. C. Chapman (1997). A Simple Theory for the Fate of Buoyant Coastal Discharges. *J. of Phys. Oceanogr. 27*, 1386–1401.

Yankovsky, A. E., B. M. Hickey, and A. K. Münchow (2001). Impact of variable inflow on the dynamics of a coastal buoyant plume. *J. of Geophys. Res. 106*(C9), 19,809–19,824.

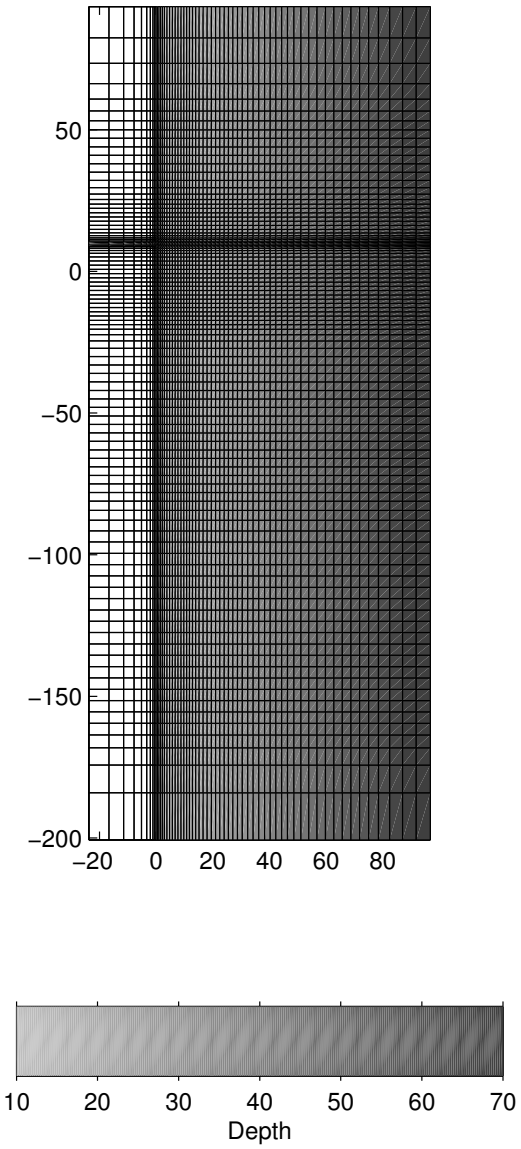

Figure 1: The model domain includes a flat-bottomed, prismatic estuary attached to a uniformly sloping coast. The shallowest depths are 10 m in the estuary and at the coast, and 70 m along the seaward edge. The model grid is focused near the estuary mouth, with 500 m resolution in this region. Moderate resolution increases gradually away from this point to 3 km, until very near the edges were it is more telescoped to much coarser resolution at the boundaries. This was done to increase the domain size, and reduce grid-scale noise at the boundaries.

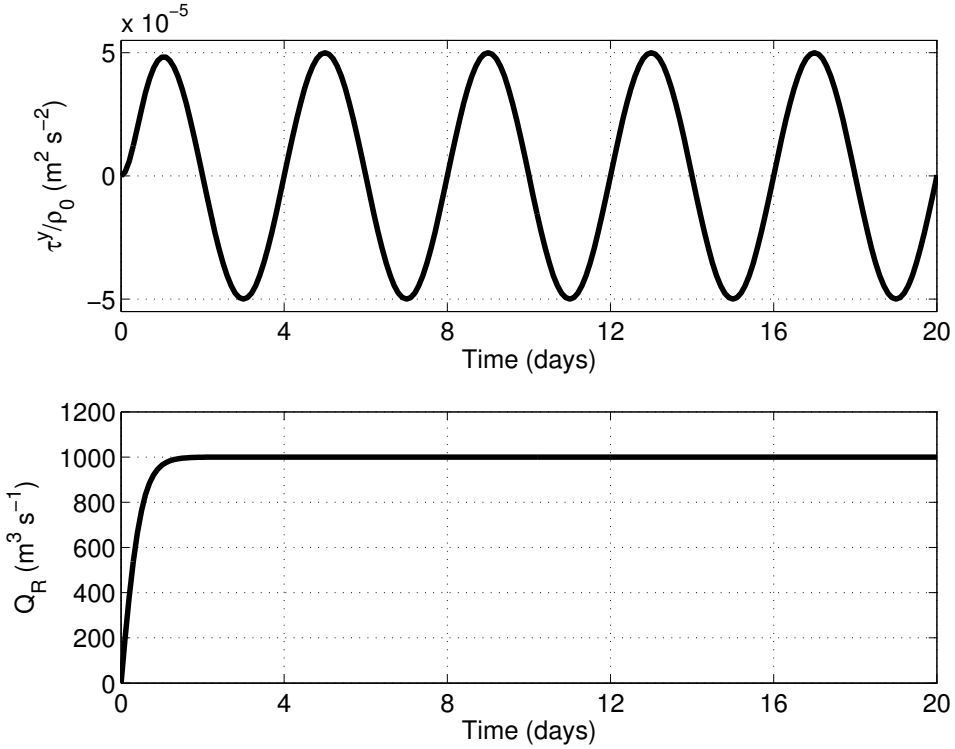

Figure 2: Model forcing includes a sinusoidal wind stress with period of four days (upper panel), and steady fresh water discharge (lower panel). Wind forcing amplitude is modified in some simulations, occasionally set to zero. Both time-series have a ramp applied, do reduce high frequency oscillations excited by suddenly turning on the forcing.

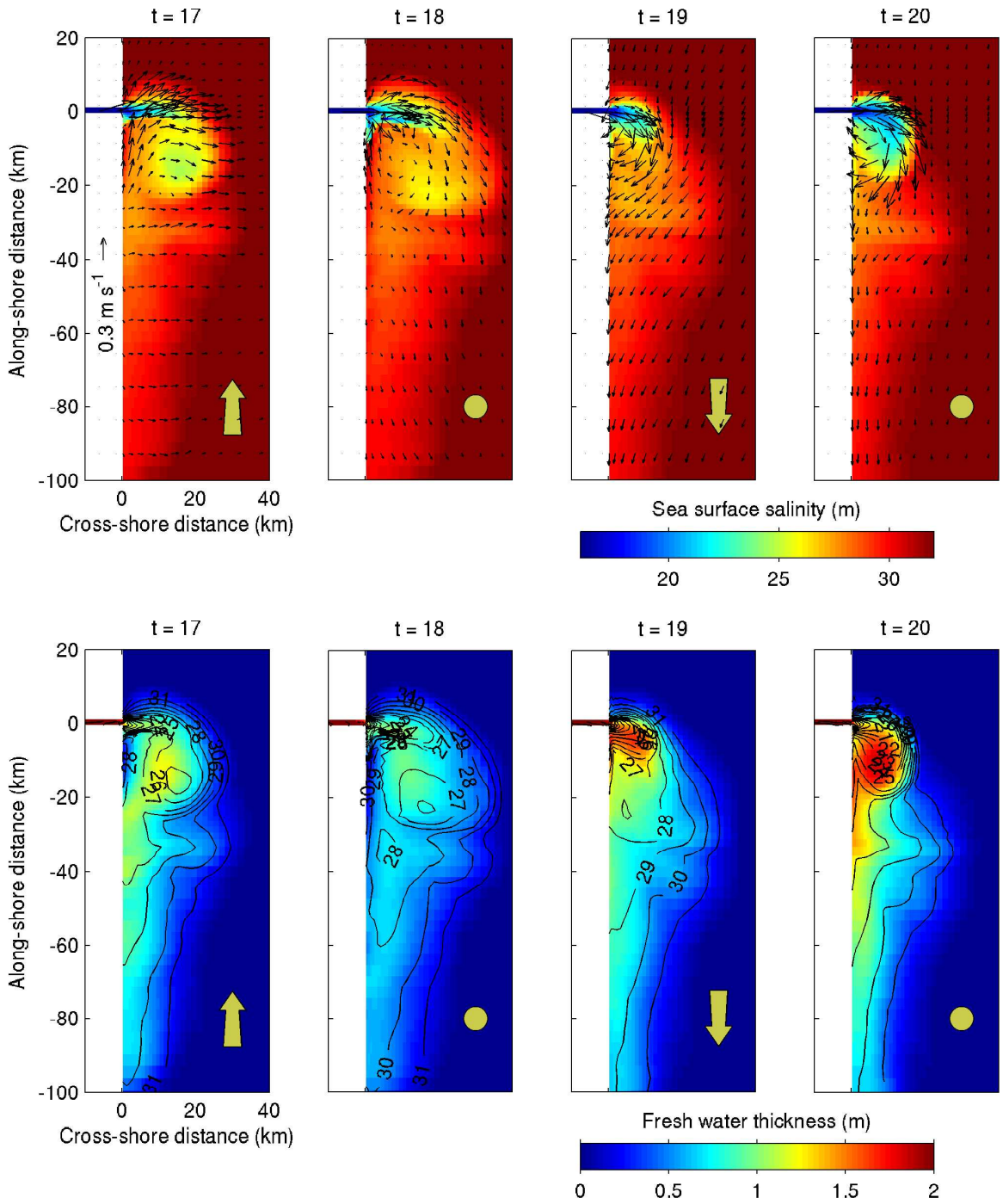

Figure 3: The sea surface salinity (upper panels) and fresh water thickness (lower panels) are plotted on a color scale for the final four days of the simulation with a wind stress amplitude of 0.5×10^{-4} m^2 s^{-2}. Instantaneous surface current vectors are overlaid on the sea surface salinity. The yellow arrow indicates the direction of the wind during maximum upwelling and downwelling; the yellow dot indicates zero wind stress at that instant. The four phases of wind stress forcing show how the structure and position of the plume changes in response to the wind.

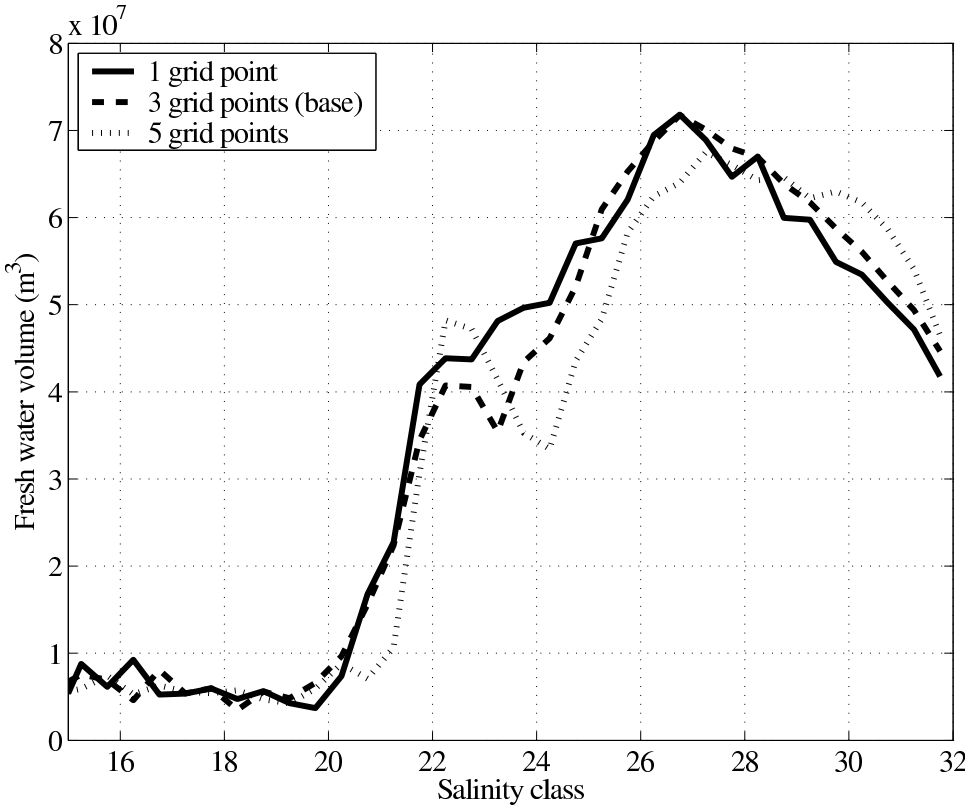

Figure 4: A comparison of $\partial V_f / \partial s_A$ as a function of salinity class, s_A, for different horizontal resolutions across the estuary mouth. Moderate (3 grid points across the estuary mouth) and high (5 grid points) resolution show similar characteristics, in particular, the show two distinct peaks in water mass structure for the near- and far-field plume. The low resolution (1 grid point) simulation does not show two distinct water masses.

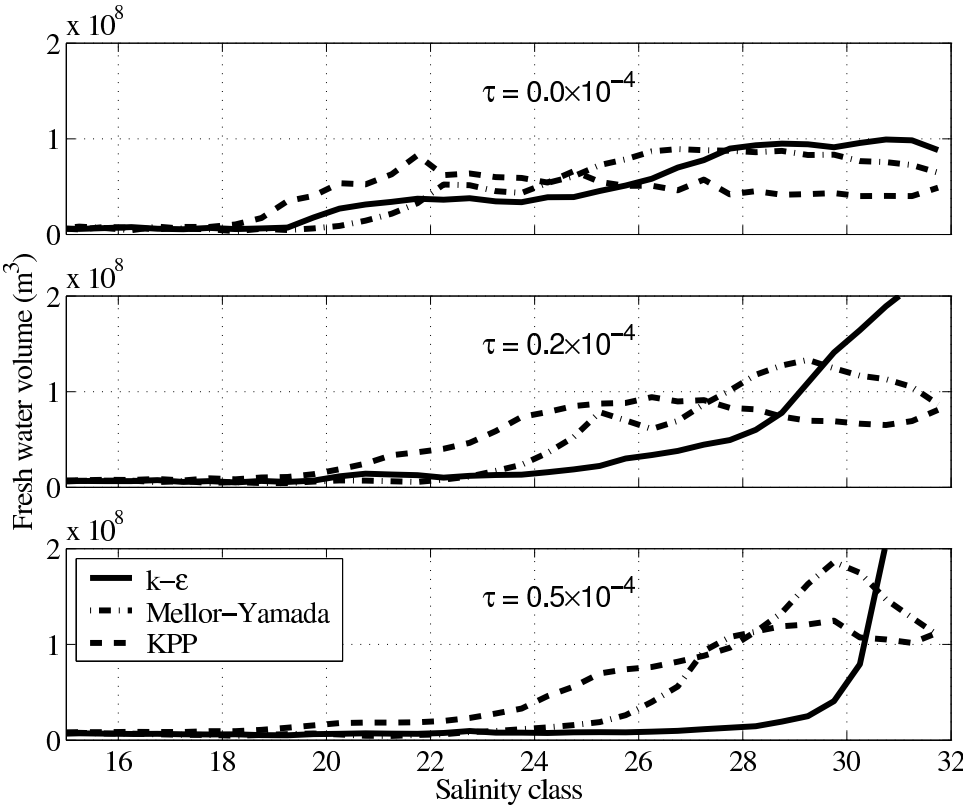

Figure 5: A comparison of $\partial V_f/\partial s_A$ as a function if salinity class, s_A, is compared for different mixing schemes under various wind forcing ($\tau_0 = 0, 0.2 \times 10^{-4}$, and 0.5×10^{-4} m^2 s^{-2}). The solutions are qualitatively similar, in that stronger wind forcing creates causes stronger mixing, pushing the fresh water toward higher salinities. However, the different mixing schemes are quantitatively different. The $k-\epsilon$ scheme mixes the most, KPP least, and Mellor-Yamada between these extremes.

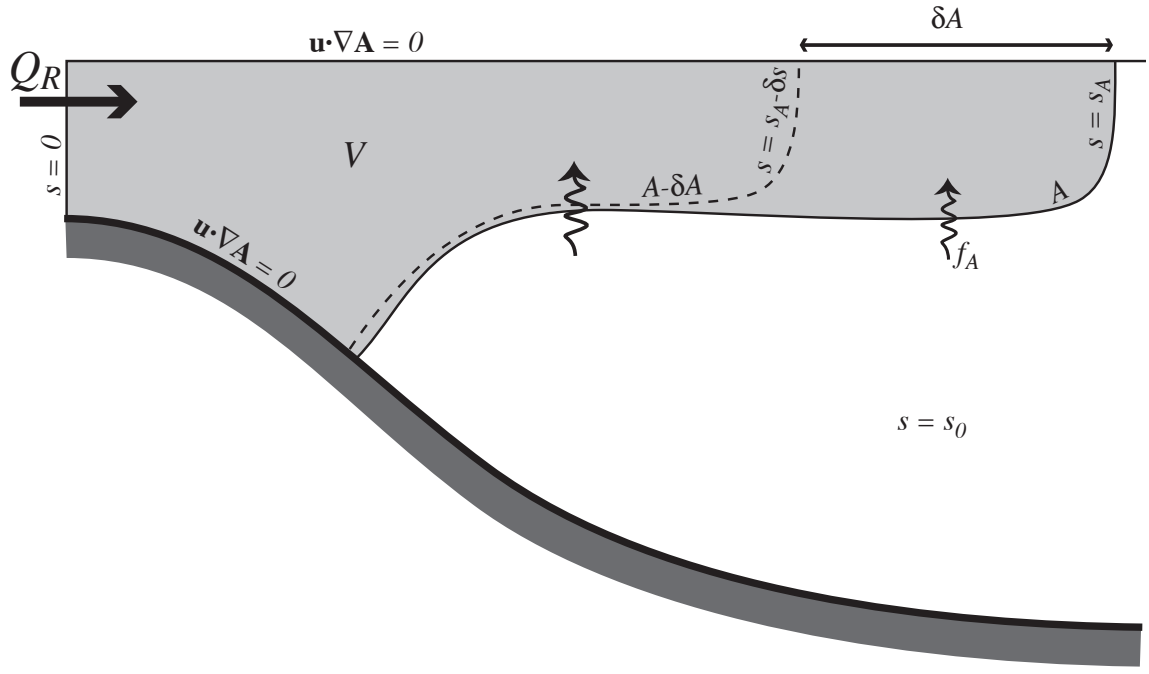

Figure 6: The volume V, bounded on the seaward edge by area A, is shaded gray; the area A is defined by isohaline $s = s_A$. A fresh water flux, Q_R, is input into the volume on the opposite face of V. Another isohalines is shown, $s_A - \delta s < s_A$ is used in an example in the text. The difference in isohaline area between $s_A - \delta s$ and s_A is δA.

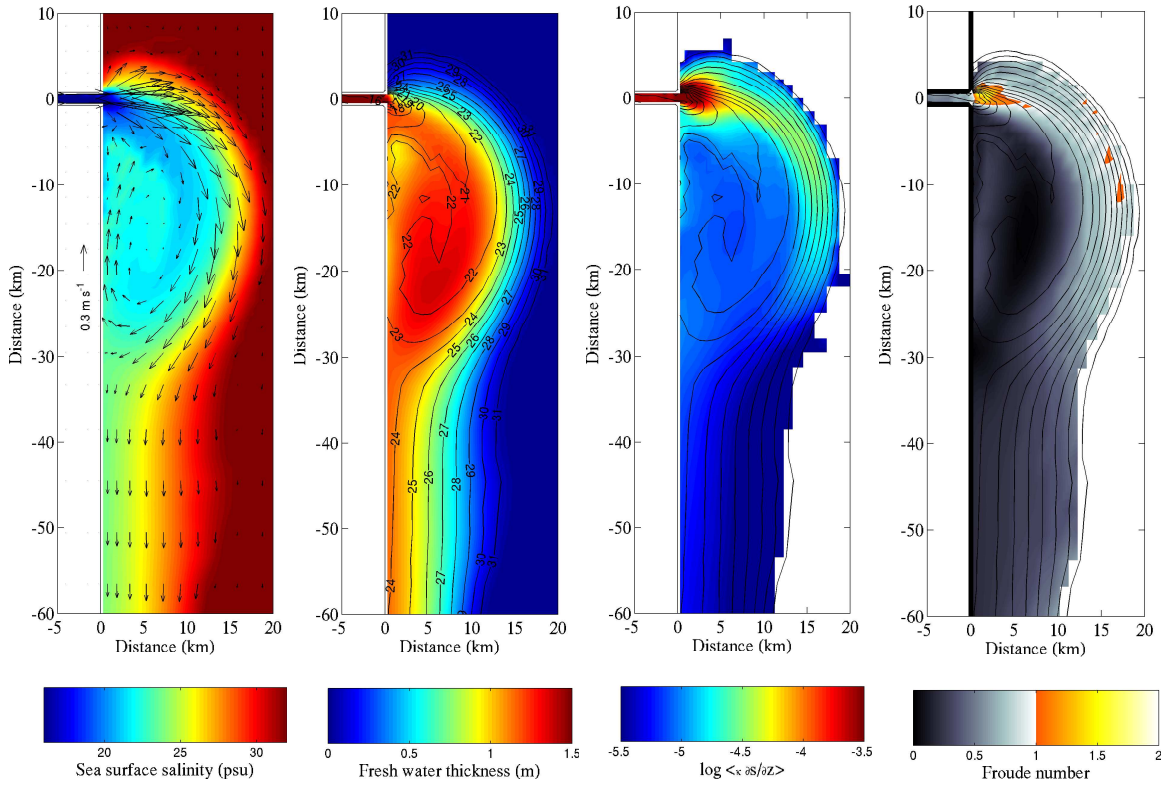

Figure 7: Four properties of the plume are shown on day 6 of the simulation without wind: sea surface salinity (with surface current vectors overlaid), fresh water thickness, a weighted average of the vertical salt flux ($\log\langle\kappa\partial s/\partial z\rangle$), and the Froude number. Property definitions are given in the text.

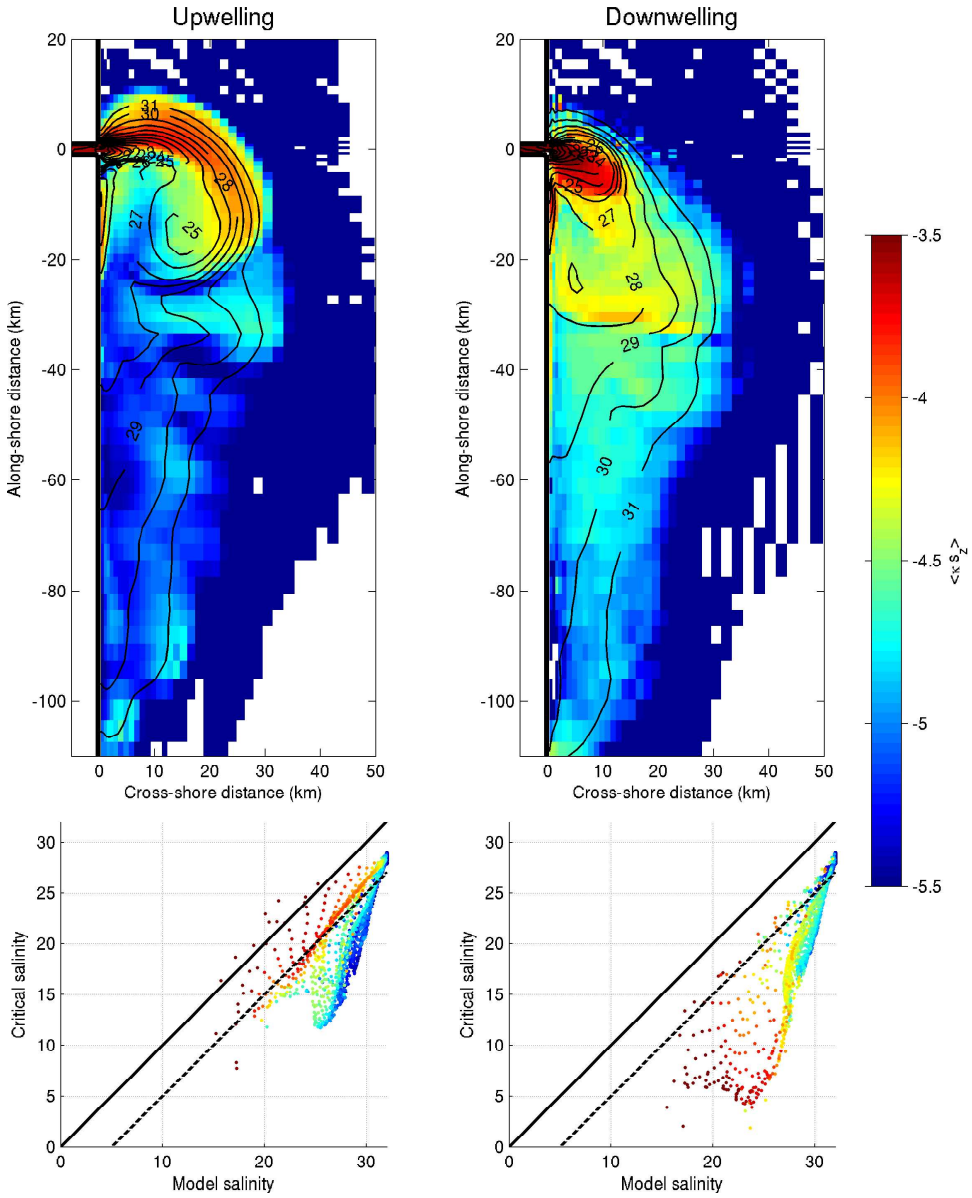

Figure 8: This figure shows the maximum vertical salt flux for extreme upwelling and downwelling winds in the upper two panels, and the corresponding critical salinity vs. the actual plume surface salinity in the lower two panels. In all panels, the logarithmic color scale represents a weighted average of the vertical salt flux ($\langle \kappa \partial s / \partial z \rangle$) for a particular horizontal point in the domain. The lower panels are based on equation 11. The solid line shows the relation $s_c = s_{model}$; the dashed line shows an offset defined by $s_c = s_{model} - 5$.

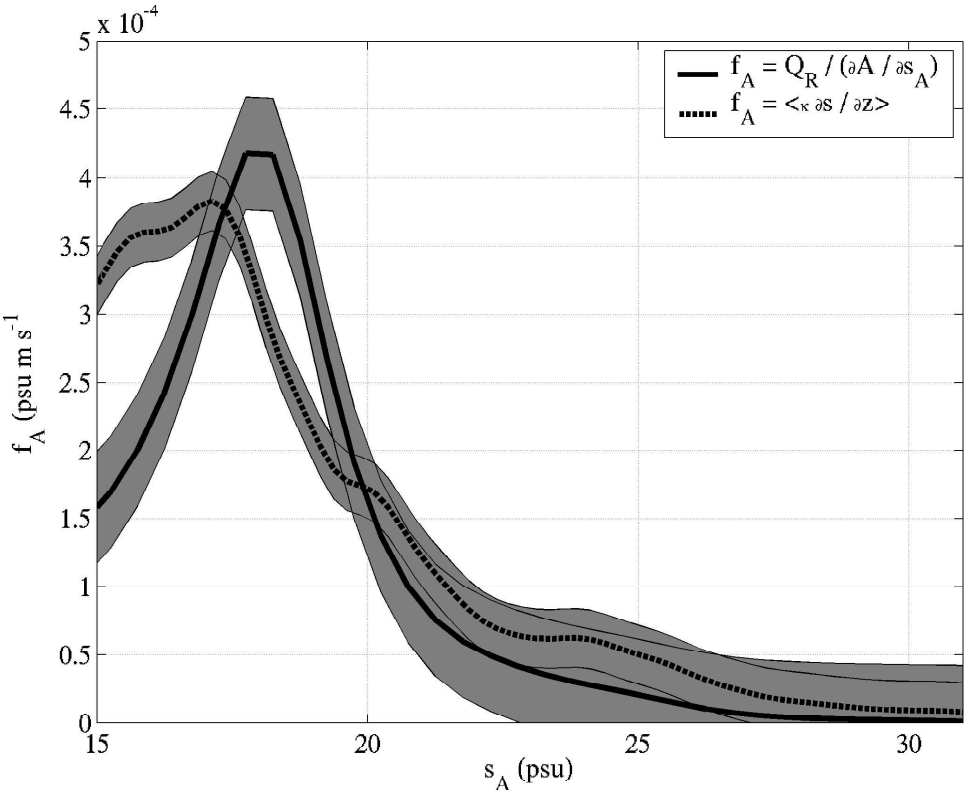

Figure 9: Two estimates of f_A, the vertical salt flux at salinity class s_A, are shown. The dashed line is $\langle \kappa \partial s / \partial z \rangle$, a weighted vertical salt flux calculated from the model. The solid line is calculated from equation 14, assuming a steady state. Both estimates have been filtered so that the resolution in salinity space is approximately 1 psu. The gray regions represent one standard deviation of the noise filtered out of each salt flux estimate.

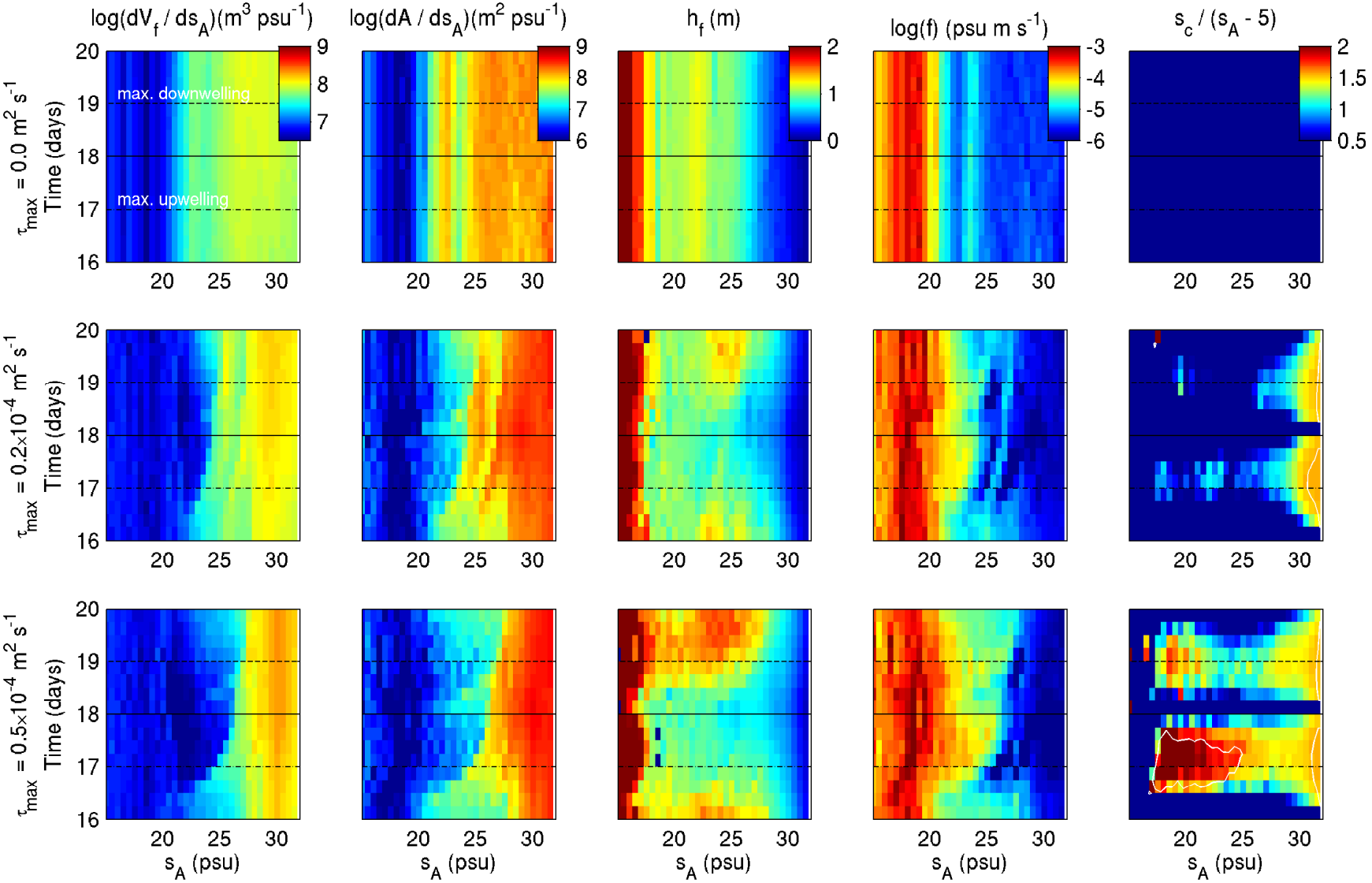

Figure 10: Five properties are plotted against salinity class, s_A ($\partial V_f/\partial s_A$, $\partial A/\partial s_A$, the fresh water thickness h_f, a weighted average of the vertical salt flux $\langle \kappa \partial s/\partial z \rangle$, and the critical surface salinity s_c) for three different wind stress magnitudes ($\tau_0 = 0, 0.2 \times 10^{-4}$, and 0.5×10^{-4} m^2 s^{-2}). The final three properties represent average values for a sea surface salinity equal to s_A. The horizontal lines represent the phase of the along-shore wind stress, the same times as the panels in figure 2.

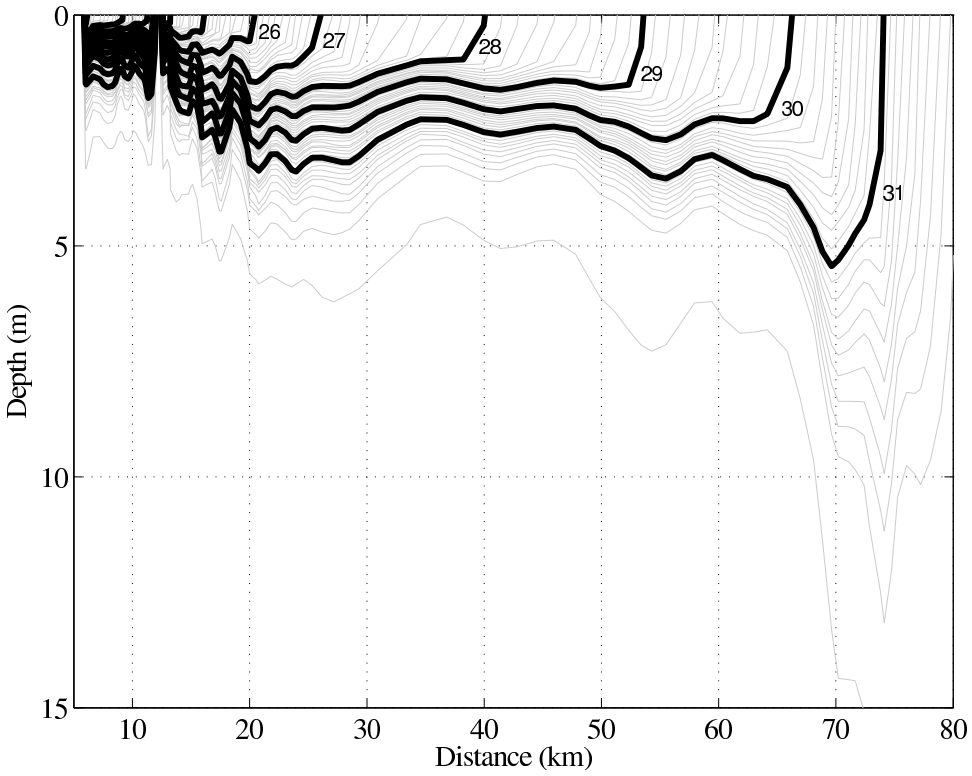

Figure 11: The average vertical salinity structure as a function of sea surface height was calculated. The methods used to create this figure are described in text. The average salinity over one wind forcing period (16 to 20 days) was used in for this particular calculation, and the isohaline depth was horizontally averaged with a 1-2-1 filter.

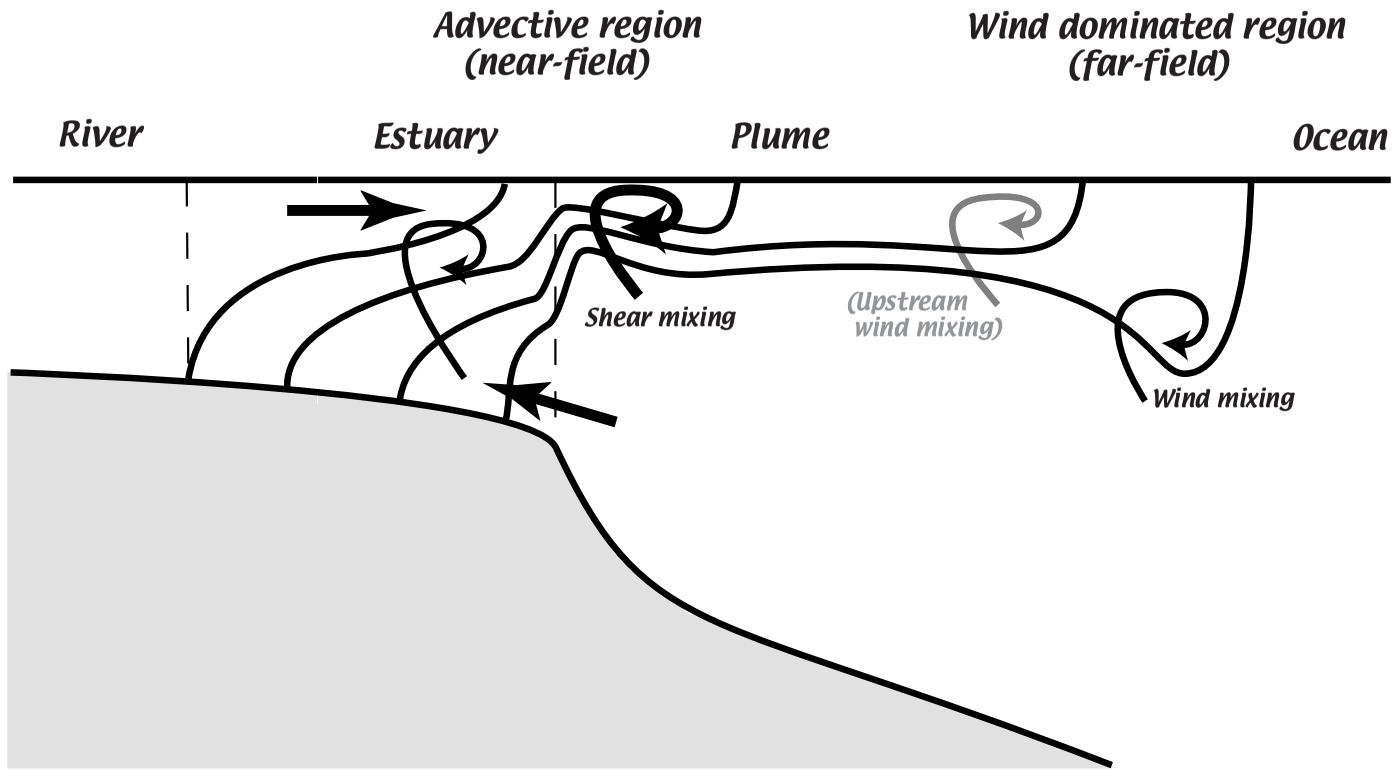

Figure 12: This conceptual model of river plume anatomy shows the major regions and indicates the dominant mixing mechanisms.